Available online at www.sciencedirect.com
ScienceDirect
Trans. Nonferrous Met. Soc. China 32(2022) 2339−2352
Transactions of Nonferrous Metals Society of China
www.tnmsc.cn

Influence of interface morphology on dynamic behavior and energy dissipation of bi-material discs

Zi-long ZHOU, Jian-you LU, Xin CAI, Yi-chao RUI

School of Resources and Safety Engineering, Central South University, Changsha 410083, China

Received 9 June 2021; accepted 21 December 2021

Abstract: To investigate the dynamic behavior and energy dissipation of the rock−concrete interface, dynamic splitting tests on bi-material discs were conducted by using the split Hopkinson pressure bar. The test results reveal that with the change of the interface inclination angles (θ), the influence of interface groove width on the bearing capacity of specimens also varies. When θ increases from 0° to 30°, the bearing capacity of the specimen increases first and then decreases with the rise of the interface groove width; the optimal groove width on the rock surface in this range of interface inclination angles is 5 mm. When θ increases from 45° to 90°, the bearing capacity of the specimen has no obvious change. Moreover, when θ increases from 0° to 45°, the dissipated energy of the specimens rises obviously at first and then tends to be stable as the width of the interface groove increases.

Key words: rock−concrete interface; Brazilian disc splitting; fracture development; interface mechanical properties; dynamic behavior; energy dissipation

1 Introduction

Concrete is commonly poured on the rock to maintain the stability of bedrock in engineering projects such as tunnel support [1−4], arch bridge foundations [5], nuclear waste storage [6], retaining walls [7−9], rock-socketed piles [10−12] and concrete dam [13,14]. However, due to the weak mechanical properties of the interface between rock and concrete, structural failure often occurs at the interface [15−18]. To ensure safety in engineering construction, the mechanical properties of the rock−concrete interface are urgent to be investigated.

In recent years, research on mechanical properties of the rock−concrete interface has been widely studied by compression tests [19−21], tension tests [22−29] and shear tests [5,10,30−35]. For example, SHEN et al [35] investigated the effect of interface roughness on the bond performance of granite−concrete interface under inclined shear conditions. It was found that the interface bond strength of the rock−concrete interface rises with the increase of its roughness. HONG et al [21] explored the bonding behavior between the rock and the mortar interface, and pointed out that the bonding force of the interface first rises and then tends to be stable with the increase of surface roughness. CHANG et al [26] studied the influence of groove depth on the mechanical properties of the rock−concrete interface. Their results showed that with the increase of the groove depth, the bonding performance of the rock−concrete interface first increases and then tends to be stable.

The environmental conditions of the above-mentioned studies are limited to quasi-static conditions; however, the rock−concrete interface is often subject to dynamic loading in situ conditions,

Corresponding author: Jian-you LU, Tel: +86-13283913031, E-mail: jianyou.lu@csu.edu.cn
DOI: 10.1016/S1003-6326(22)65951-X

such as earthquakes and blasting [36−39]. LUO et al [40] first conducted high strain rates tests on the bi-material specimens and investigated the influence of the rock surface sawtooth depth on the dynamic mechanical properties of the rock−concrete interface by using a split Hopkinson pressure bar (SHPB) apparatus. They reported that the peak load of the specimens rises first and then decreases with the increase of sawtooth depth. However, the loading and interface direction were parallel in their work, the effects of the inclined angle of the interface were ignored. In addition to increasing the groove depth in their study, the groove width can be increased to improve the bond performance of the rock-concrete interface. Increasing the groove depth simply improves the tensile properties of the interface, while increasing the groove width can improve tensile properties and shear properties of the interface. In practical engineering, tensile load and shear load are frequently encountered. Therefore, the optimal groove width at the interface should be studied in the structure containing a rock−concrete interface to improve the tensile and shear strength of the interface.

In this study, the influence of interface morphology on the dynamic behavior and energy dissipation of the rock−concrete interface exposed to dynamic loads was investigated. To obtain the optimal groove width under different interface inclination angles, the rock−concrete bi-material discs with different interface groove widths were manufactured; the dynamic splitting tensile tests and the quasi-static splitting tensile tests on these specimens were performed under different inclined angles. The fracture development process, bearing capacity and deformation of the specimens after these two tests were compared. During these tests, a high-speed (HS) camera was used to capture the failure processes of specimens. Finally, the influence of interface inclination angle and the interface groove width on the mechanical properties, failure pattern, and energy dissipation of the rock−concrete bi-material discs was revealed.

2 Experimental

2.1 Specimen preparation

In this work, the limestone collected from Jiaozuo (Henan province, China) was taken as rock specimen. The concrete was made up of cement, sand, gravel and water with a mass ratio of 1: 0.63: 0.95:0.40. Figure 1 shows the grading curve of gravel and sand of concrete aggregate, and Table 1 shows the basic mechanical parameters of the limestone and the concrete.

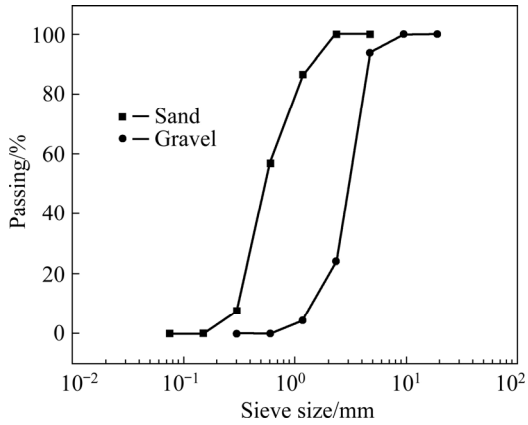

Fig. 1 Grading curves of gravel and sand of concrete aggregate

Table 1 Basic mechanical parameters of pure rock and concrete

Material	Uniaxial compressive strength, σ_c/MPa	Static tensile strength, σ_{st}/MPa	Dynamic tensile strength, σ_{dt}/MPa
Limestone	170.40	4.83	30.25
Concrete	55.30	2.06	17.57

The rock−concrete bi-material specimens were manufactured as follows: (1) the surface of limestone slates was cleaned; (2) to change the bonding performance between rock and concrete, three types of grooves with different widths (3.0, 5.0 and 8.0 mm) and the same depth (4.0 mm) and spacing (4.0 mm) were fabricated on the surface of limestone slates; (3) the slurry of concrete was evenly poured on the surfaces of the limestone slates with different grooves as shown in Fig. 2; (4) the limestone−concrete composites were cured

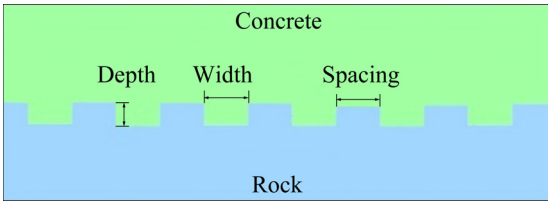

Fig. 2 Schematic diagram of rock−concrete interface groove

in the curing box for 28 d at the constant temperature of 25 °C and the humidity of 95%; (5) the bi-material discs with a diameter of 50 mm and a length of 25 mm were cored and sliced from the limestone−concrete composite slates, as shown in Fig. 3. Finally, a total of 36 bi-material disc specimens were manufactured, among which 15 specimens were used for quasi-static loading tests and 21 specimens for dynamic loading tests. Table 2

(a) (b) (c)

Fig. 3 Photographic views of specimens with different groove widths: (a) 3.0 mm; (b) 5.0 mm; (c) 8.0 mm

Table 2 Parameters for test specimens

Test condition	Specimen No.	Groove size (width × depth × spacing)/mm	Interface inclination, θ/(°)	Diameter/ mm	Height/ mm	Peak force/ kN
Quasi-static	SA-0	3.0 × 4.0 × 4.0	0	49.62	25.95	2.32
	SA-15		15	49.15	25.70	3.69
	SA-45		45	49.37	25.44	6.43
	SA-60		60	49.81	27.05	7.03
	SA-90		90	49.38	27.31	11.72
Quasi-static	SB-0	5.0 × 4.0 × 4.0	0	49.52	26.73	3.07
	SB-15		15	49.27	26.49	6.32
	SB-45		45	49.65	26.17	8.28
	SB-60		60	49.38	25.39	7.71
	SB-90		90	49.63	25.45	8.06
Quasi-static	SC-0	8.0 × 4.0 × 4.0	0	49.86	25.67	3.08
	SC-15		15	49.17	25.96	4.88
	SC-45		45	49.69	25.54	7.62
	SC-60		60	49.38	26.53	8.52
	SC-90		90	49.14	25.74	7.67
Dynamic	DA-0	3.0 × 4.0 × 4.0	0	49.38	25.55	22.36
	DA-15		15	49.68	25.29	27.83
	DA-30		30	49.55	25.66	28.78
	DA-45		45	49.28	25.62	38.45
	DA-60		60	49.61	26.49	40.91
	DA-75		75	49.37	25.30	45.04
	DA-90		90	49.27	25.33	42.81
Dynamic	DB-0	5.0 × 4.0 × 4.0	0	49.91	25.90	32.14
	DB-15		15	49.85	24.42	32.63
	DB-30		30	49.71	25.85	39.31
	DB-45		45	49.93	25.30	39.68
	DB-60		60	49.61	25.90	38.09
	DB-75		75	49.53	26.00	39.77
	DB-90		90	49.16	25.35	46.01
Dynamic	DC-0	8.0 × 4.0 × 4.0	0	49.26	26.86	24.13
	DC-15		15	49.38	25.56	26.98
	DC-30		30	49.78	25.36	30.41
	DC-45		45	49.25	27.31	41.49
	DC-60		60	49.38	26.29	43.51
	DC-75		75	49.56	26.28	46.19
	DC-90		90	49.53	26.82	47.41

lists the detailed parameter of the specimens. As for the specimen number, the first letter of S or D represents the static or dynamic loading conditions; the second letter of A, B or C represents the groove width of 3.0, 5.0 or 8.0 mm; the last number represents the interface inclination angle (θ). For example, specimen SA-0 represents the specimen with a groove width of 3.0 mm and an interface inclination angle of 0° tested under the static loading.

2.2 Experimental setup

2.2.1 Quasi-static testing system

The quasi-static loading tests were carried out on a servo-controlled material testing machine (MTS 322) located in the Advanced Research Center of Central South University, Changsha, China (see Fig. 4). The maximum load-carrying capacity and load control accuracy of the MTS 322 were 500 kN and 0.5%, respectively. Before the test, the lubricant was applied to the ends of the specimen to reduce the end friction. The loading rate during the entire loading process was kept at 50 kPa/s.

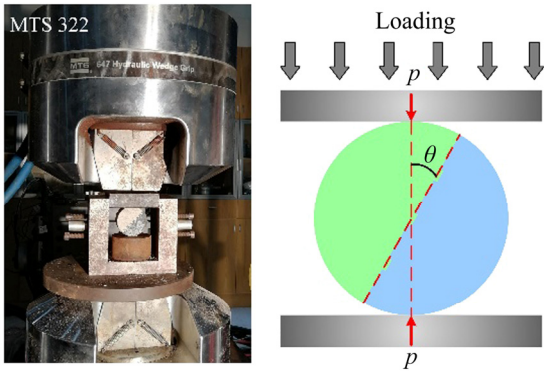

Fig. 4 Quasi-static test system: (a) Photographic view; (b) Schematic illustration

2.2.2 Split Hopkinson pressure bar system

The dynamic loading tests were performed on an improved split Hopkinson pressure bar (SHPB) system in the Central South University (see Fig. 5). The SHPB apparatus can generate a half-sine stress wave to eliminate PC oscillation and achieve stress equilibrium (see Fig. 6) [41−43]. The detailed principle and operation procedures are available in previously study [44]. To compare the effect of interface morphology on dynamic behavior and energy dissipation of specimens, the loading rates of all specimens in dynamic tests are nearly 900 GPa/s.

2.2.3 HS photography system

An HS photography system was used to record the fracture development of the bi-material disc specimen. As shown in Fig. 5, the high-speed photography system consists of a high-speed camera (FASTCAM SA1.1) and a high-intensity spotlight (Pallite VIII). The high-speed camera took 72000 frames per second in 256 × 240 pixels. The camera was triggered by a TTL pulse emitted from the oscilloscope when the voltage of the incident wave reached −34 mV.

2.3 Data reduction

2.3.1 Dynamic loading in SHPB test

The dynamic loads at the contact points between the specimen and bars can be calculated by [45]

$$F_1(t)=EA[\varepsilon_i(t)+\varepsilon_r(t)] \quad (1)$$

$$F_2(t)=EA\varepsilon_t(t) \quad (2)$$

where $F_1(t)$ is the force at the contact point of the incident bar and the specimen; $F_2(t)$ is the force at the contact point of the transmission bar and the specimen; A is the cross-sectional area of the bar; E

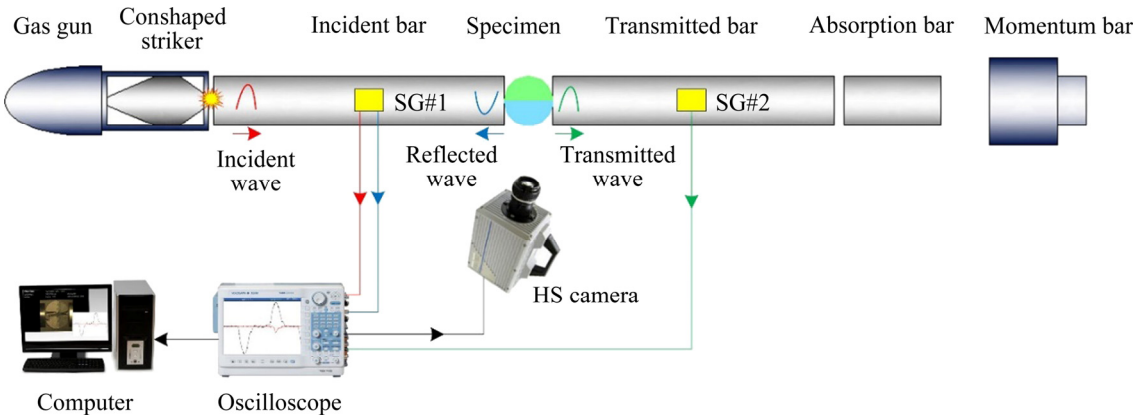

Fig. 5 Split Hopkinson pressure bar system

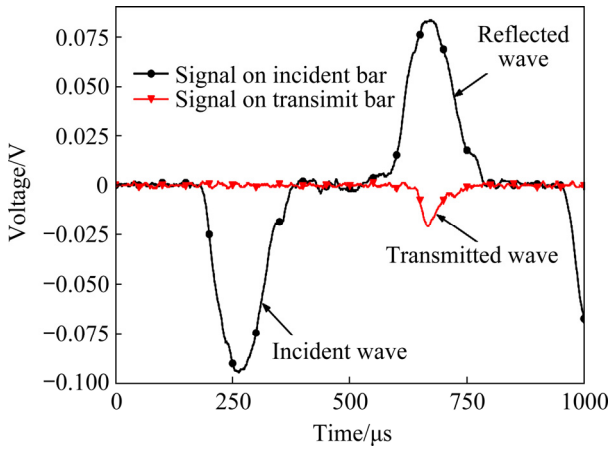

Fig. 6 Typical signals recorded by strain gauge

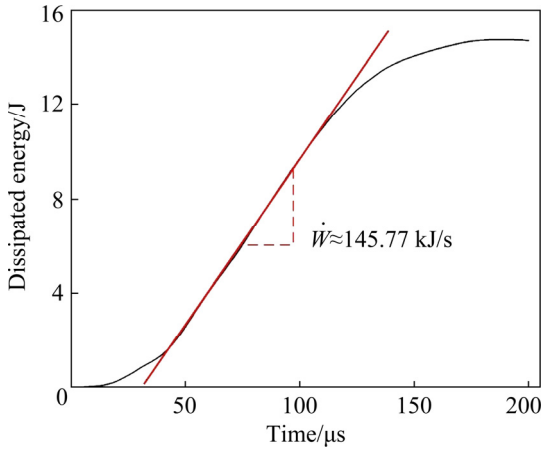

Fig. 7 Dissipated energy−time curve

is the elastic modulus of the bar; $\varepsilon_i(t)$ is the incident strain; $\varepsilon_r(t)$ is the reflected strain; $\varepsilon_t(t)$ is the transmission strain.

When the force balance is fulfilled, the average loading force $F(t)$ at both ends of the specimen can be calculated by [46,47]

$$F(t)=\frac{F_1(t)+F_2(t)}{2} \tag{3}$$

2.3.2 Dissipated energy and energy dissipation rate

In SHPB tests, if the energy consumption at the contact among the specimen, bars and heat energy is ignored, the dissipated energy (W_s) of the specimen during the loading process is obtained as follows [48]:

$$W_s=W_I-(W_R+W_T) \tag{4}$$

where W_I, W_R and W_T are the elastic strain energy induced by the incident wave, reflected wave and transmitted wave, respectively. These elastic strain energies can be calculated by

$$\begin{cases} W_I = ACE\int \varepsilon_i(t)^2\,\mathrm{d}t \\ W_R = ACE\int \varepsilon_r(t)^2\,\mathrm{d}t \\ W_T = ACE\int \varepsilon_t(t)^2\,\mathrm{d}t \end{cases} \tag{5}$$

where C is the P-wave velocity of the bar.

Figure 7 shows a typical dissipated energy−time curve of the bi-material disc specimen during the dynamic loading. The curve is S-shaped. In the middle section, the energy dissipation increases almost linearly with time, indicating that the energy consumption of the specimen is stable at this stage. The slope of the linear portion is defined as the energy dissipation rate ($\dot{W}$).

3 Test results

3.1 Fracture development process and failure pattern of specimens

Figure 8 shows the typical failure process of the specimens. For Specimen DA-0 (the groove width is 3.0 mm and the interface inclination angle is 0°), the crack first occurs in the center of the disk at 14 μs. At 28 μs, the main cracks develop along the rock−concrete interface towards the loading end of bars. The main cracks at the interface penetrate the specimen at 98 μs, and the secondary cracks also appear at the interface. At 714 μs, the specimen totally loses its bearing capacity and reaches a complete failure state. For the Specimen DA-15 (groove width is 3.0 mm, interface inclination is 15°), the cracks firstly appear along the interface at 14 μs. At 28 μs, the wing cracks appear in the loading ends. At 56 μs, the wing crack develops to the end. At 308 μs, the specimen is completely destroyed; the rock and concrete slide in opposite directions along the interface, that is, the phenomenon of shear dislocation occurs. However, for the Specimen DC-15 (the groove width is 8.0 mm, the interface inclination angle is 15°), as the groove width increases, the crack firstly occurs near the center of the disk at 14 μs. At 126 μs, the crack penetrates the entire specimen. At 532 μs, the specimen fails completely and the rock sawtooth is fractured. For the Specimen DA-60 (the groove width is 3.0 mm, the interface inclination angle is 60°), the crack first appears in the center of the disc specimen at 14 μs. At 42 μs, the cracks develop to both ends of the specimen along the loading direction. At 140 μs, cracks appear at the rock−

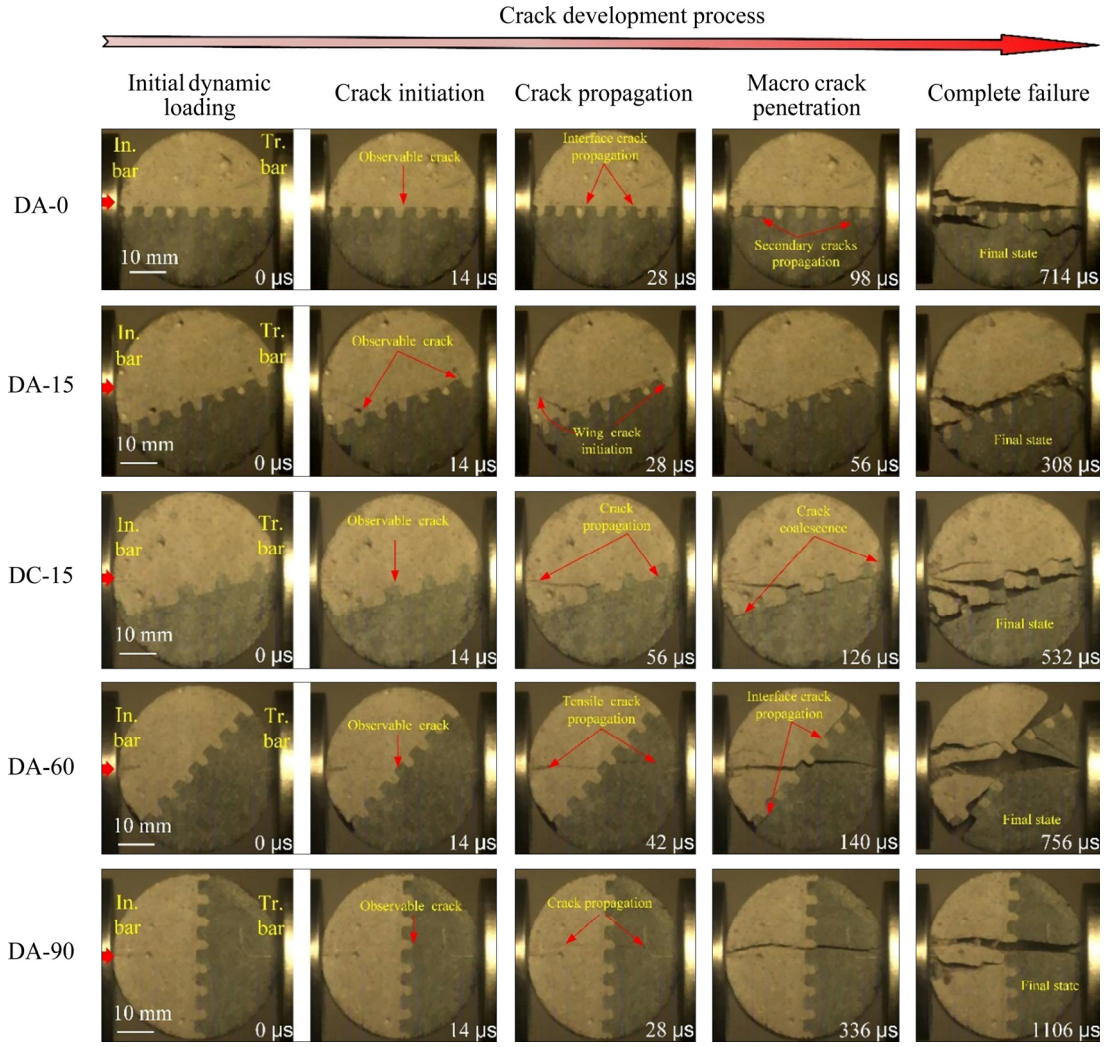

Fig. 8 Fracture development process of typical failure pattern of specimens

concrete interface. At 756 μs, the specimen fails completely. For the Specimen DA-90 (the groove width is 3.0 mm, and the interface inclination angle is 90°). At 14 μs, the crack first appears in the center of the disc specimen. At 28 μs, the main crack develops toward the end of the specimen along the loading direction. At 336 μs, the crack penetrates the specimen. At 1106 μs, the specimen fails completely. At the same time, secondary cracks also appear near the incident end of the specimen along the loading direction.

Figure 9 shows the failure patterns of the bi-material disc specimen after the test. Figures 9(a) and (b) show the failure patterns of the specimens under the static and dynamic loads, respectively. When the inclination angle of the specimen is 0° (such as SA-0 and DA-0), the specimens with different groove widths have the similar failure patterns, i.e., cracks are generated in the loading direction. This failure pattern is the same as that of brittle materials (such as pure rock or pure concrete) under the classic Brazilian split test. The reasons are as follows: when the Brazilian disc is loaded along the radial direction, the tensile stress inside the disc will first reach the maximum tensile strength of brittle materials such as rock; in the classical Brazilian split test of brittle materials cracks are developed along the loading direction in the bi-material disc, the interface serves as the weaker part of the disc specimen, and the cracks are also generated along the interface once the loading direction is the same as the interface.

When the inclination angle of the interface is 15° and the groove width is small (such as SA-15 and DA-15), the failure occurs along the interface, and the rock sawtooth at the interface is not destroyed at this time. However, when the groove width is large (such as SC-15 and DC-15), although

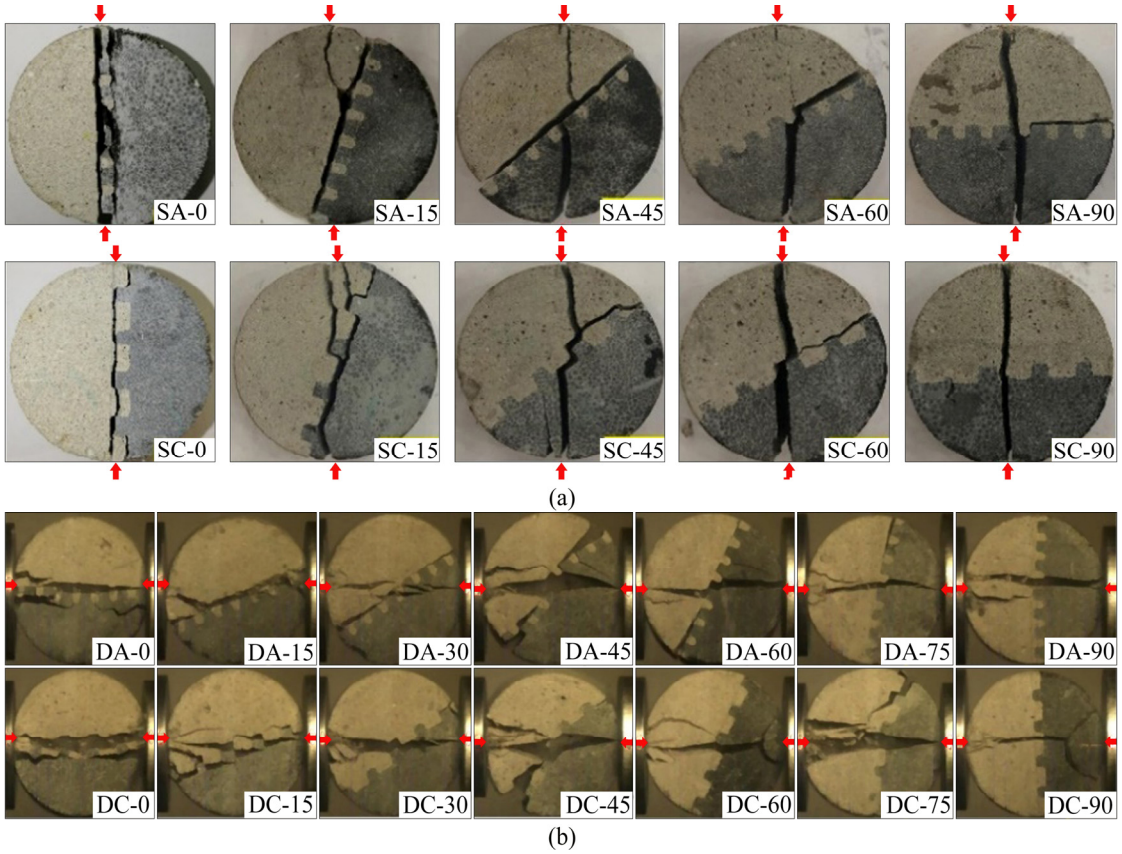

Fig. 9 Typical failure patterns of bi-material disc specimens with different interface groove widths and interface inclination angles: (a) Under static loading; (b) Under dynamic loading

the failure also occurs along the interface, the rock sawtooth fractures at the interface at this time.

This can be explained as follows: if the groove width of the rock is small, the width of the concrete sawtooth is smaller (the groove width of the rock is equal to the width of the concrete sawtooth), and the strength of the concrete is less than that of the rock (see Table 1). As a result, when the groove width of the rock is small, the concrete sawtooth fracture occurs at the interface; when the groove width of the rock is large, the rock sawtooth fracture occurs at the interface. In this case, the load-bearing capacity of the concrete sawtooth is less than that of the rock sawtooth. At this time (specimen SA-15 or DA-15) the width of the concrete sawtooth is only 3.0 mm, and the width of the rock sawtooth is 4 mm, so the concrete sawtooth is broken but the rock sawtooth not (such as SA-15 or DA-15). However, if the width of the rock groove is larger, the width of the concrete sawtooth is larger. At this time, the width of the concrete sawtooth is 8.0 mm, and the width of the rock sawtooth is 4 mm, then the rock sawtooth of the specimens SC-15 and DC-15 will fracture, as shown in Fig. 9.

When the interface inclination angle is in the interval of 30° to 75°, the groove width has no obvious influence on the failure pattern of the specimen. In these failure patterns cracks are produced in the rock along the interface and the loading direction. This can be explained as follows: When the bi-material disc is subjected to radial loading, tensile cracks first appear along the loading direction, which is similar to test results of the classical rock disk Brazilian splitting test. Subsequently, since the bi-material disc is split into two half disks, there is a rock−concrete interface in each half-disk; the interface acts as a weak surface, and cracks fracture along the interface after the continuous loading (such as DA-60). When the interface inclination angle is 90°, the groove width has no obvious effect on the failure pattern of the bi-material disc specimen. In this failure pattern cracks are only generated in the rock part along the loading direction, and no interface cracks are produced. It is also the only failure pattern without

interface cracks when the interface inclination angle increases from 0° to 90°. This is because when the interface inclination angle is 90°, the interface is under compression, no cracks appear along the interface, and the cracks only appear in the matrix material along the loading direction. This failure pattern is the same as that of the classic Brazilian splitting tests on the pure rock.

3.2 Deformation response of bi-material disc specimens

Figure 10(a) shows the load−displacement curves of bi-material disc specimens with different interface groove widths under static loading conditions. When the groove width is 3.0 mm (Specimen SA-15), at the initial stage of loading, as the displacement increases, the corresponding load increases approximately linearly until it reaches the peak load. After the peak load, as the displacement continues to increase, the peak load of the specimen suddenly drops to zero. The changing trend of the load−displacement curve of the specimens with the groove width of 5.0 mm (Specimen SB-15) is similar to that of the groove width of 3.0 mm (Specimen SA-15). Before the peak load, the load borne by the specimens increases approximately linearly, and after the peak load, the load suddenly drops to zero. When the groove width is 8.0 mm (Specimen SC-15), before the peak load, the load gradually rises with the increase of the displacement. After the peak load, as the displacement continues to increase, the load does not suddenly decrease to 0 but the load decreases stepwise. The reasons are as follows: when the specimen (SA-15 or SB-15) with a small groove width (3.0 mm or 5.0 mm) is loaded, cracks first appear at the interface; as the loading continues, the crack suddenly penetrates the entire specimen, and the specimen loses its bearing capacity. When the specimen (SC-15) with a large groove width (8.0 mm) is loaded, the crack first appears in the concrete; as the loading continues, the concrete first broke, and then the rock sawtooth at the interface broke. As a result, with the increase in the displacement, after the load reaches the peak load, the load presents a stepped drop. Figure 10(b) shows the load−displacement curves under dynamic loading conditions. It can be seen from the DA-15 curve that at the initial stage of loading, as the specimen loading displacement increases, the load

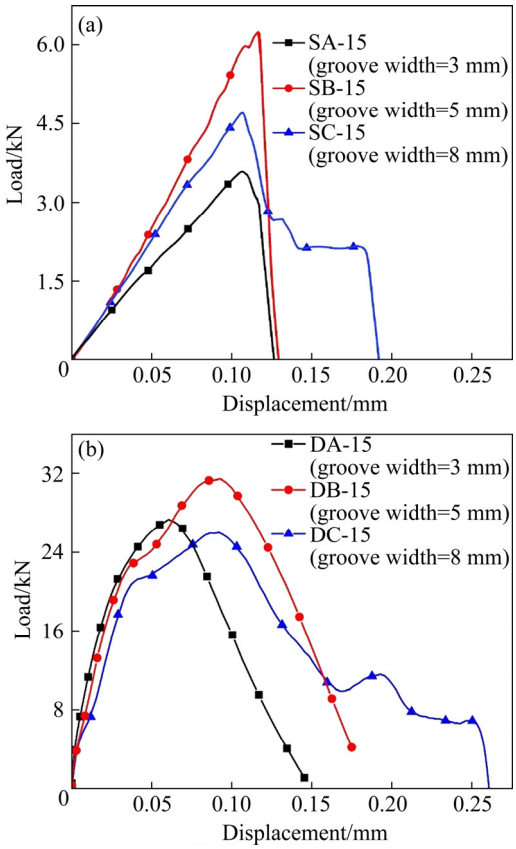

Fig. 10 Load−displacement responses under quasi-static loading (a) and dynamic loading (b)

approximately increases linearly. After the peak load, as the loading displacement increases, the load approximately decreases linearly. The load−displacement relationship curves of DB-15 and DA-15 have similar changing trends. However, after the peak load of the DC-15 curve, with the increase of the loading displacement, the peak load also has a stepwise decrease (similar to the SC-15 curve in Fig. 10(a)).

3.3 Peak load of bi-material disc specimens

Figure 11(a) shows the relationship between different groove widths on the rock surface and the peak load of the specimen under static loading. When the inclination angle is between 0° and 45° and the groove width is 3.0 mm, the corresponding peak load is the minimum. When the groove width is increased to 5.0 mm, the peak load of the specimen increases significantly (the load with an interface inclination angle of 0°, 15° and 45° increases by 33%, 71% and 29%, respectively). However, when the groove width is increased to 8.0 mm, the peak load does not continue to increase (the load with interface inclination angle of 0°, 15°

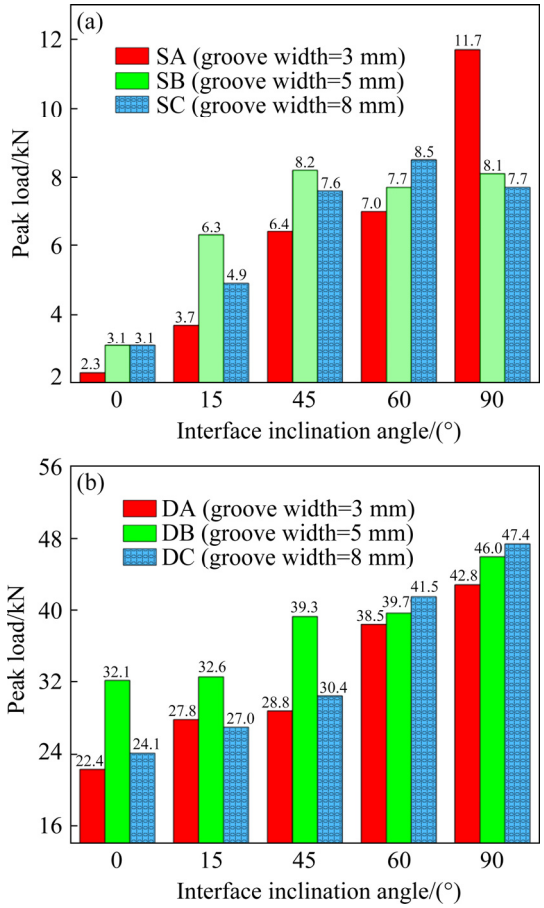

Fig. 11 Static and dynamic peak load with different groove widths under static loading (a) and dynamic loading (b)

and 30° decreases by 8%, 23% and 0%, respectively). The reason is that properly increasing the groove width of the rock surface can improve the mechanical bite between rock and concrete, so as to enhance the bond performance of the rock−concrete interface; however, the excessive groove width of the rock surface can damage the bedrock, which is not conducive to improving the bond performance of the rock−concrete interface. When the inclination angle is 60°, the width of the groove has little effect on the peak load of the specimen (with the increase of the groove width, the variation of the adjacent peak load is 10%). This is because the failure crack appears in the matrix material first, and the peak load is determined by the bearing capacity of pure rock and concrete, while the width of the interface groove has little effect on the bearing capacity of the specimen.

Figure 11(b) shows the relationship between the peak load of the specimen and the different groove widths on the rock surface under the dynamic loading. When the inclination angle is in the interval of [0°, 30°], and the groove width is 3.0 mm, the corresponding peak load is the smallest. When the groove width is increased to 5.0 mm, the peak load of the specimen with an interface inclination angle of 0°, 15° and 30° increases significantly by 44%, 17% and 37%, respectively. However, as the groove width further increases to 8.0 mm, the peak load of the specimen with an interface inclination angle of 0°, 15° and 30° decreases by 25%, 17% and 23%, respectively. This is because appropriately increasing the groove width of the rock surface can improve the mechanical occlusion between the rock and the concrete, so as to achieve the purpose of enhancing the bonding performance of the rock−concrete interface; however, the excessive groove width on the rock surface can damage the rock, which is not conducive to improving the rock−concrete bonding performance. When the inclination angle is in the interval of [45°, 90°], the groove width has little effect on the peak load of the specimen (as the groove width increases, the adjacent peak load changes are between 3% and 7%). The reason is that at this time, the failure cracks of the specimen first appear in the matrix material, and the peak load is determined by the bearing capacity of pure rock and concrete materials, while the width of the interface groove has little effect on the bearing capacity of the specimen.

Figure 12 shows the relationship between peak load of specimens and interface inclination angle under dynamic loading. As shown in Fig. 12, the peak load increases with the increase of the interface inclination angle regardless of the groove

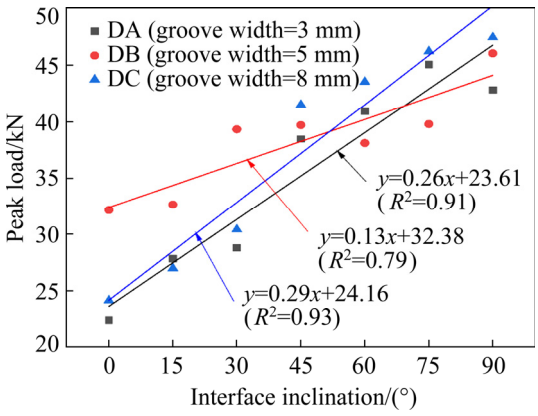

Fig. 12 Relationship between peak load and interface inclination for bi-material disc specimens under dynamic loading

width of 3, 5 or 8 mm. The results of linear regression analysis show that the slope of the regression line of the specimen with the groove width of 3, 5 and 8 mm is 0.26, 0.13 and 0.29, respectively. The slope of the regression line of the specimen with the groove width of 5 mm is the smallest. The reason is that when the inclination angle of the interface is 0° or 15°, the specimen will fracture along the rock−concrete interface; at this time, the load-bearing capacity of the specimen with the groove width of 5 mm is larger, so the slope of its regression line is the smallest in the regression analysis.

3.4 Energy dissipation of specimens

Figure 13 shows the evolution curves of the dissipation energy of specimens during dynamic loading with time. The evolution process of dissipated energy can be divided into three stages: compaction stage, linear growth stage and plateau stage. In the compaction stage, the energy is mainly used for the compaction of the original pores and micro-cracks in the specimen, which is similar to the compaction stage of the rock in the uniaxial

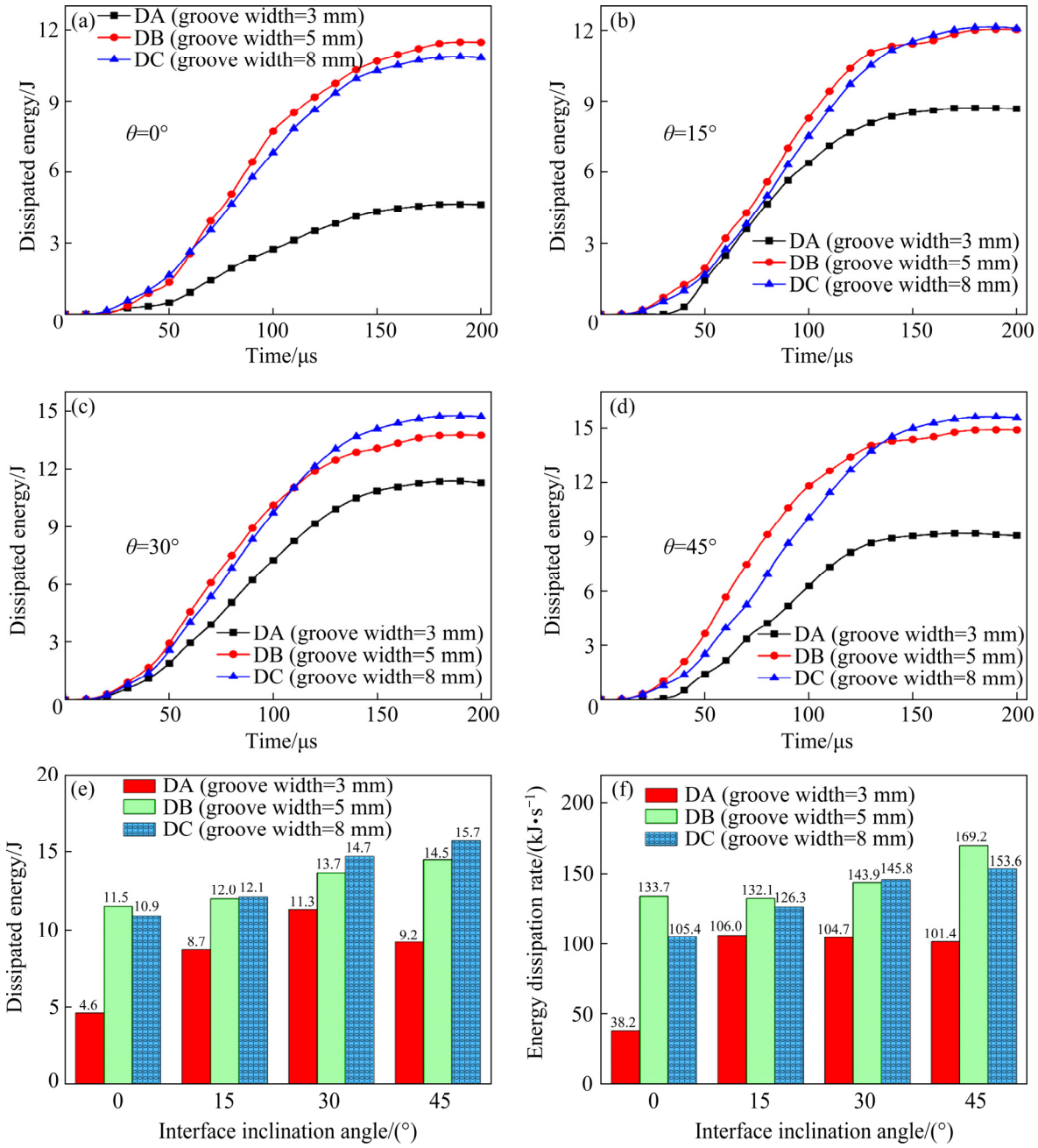

Fig. 13 Dissipated energy of rock−concrete bi-material discs under dynamic loading conditions: (a−d) Evolution process of dissipated energy with time; (e) Dissipated energy; (f) Energy dissipation rate

compression test. At the linear growth stage, the energy is quickly accumulated to generate new cracks and merge the original cracks. At the plateau stage, the energy is minimally increased because the main crack has been formed. As shown in Fig. 13, when the groove width is 3.0 mm, the energy dissipation and energy dissipation rate are the smallest. The reason may be that when the groove width on the rock surface is small, then the width of the concrete sawtooth at the rock−concrete interface is also relatively small; when $0° \leq \theta \leq 45°$, interface cracks of the specimens all appear. Besides, when the groove width is 3.0 mm (the black curve in Fig. 13), the interfacial cracks are all formed by the sawtooth fracture of concrete, and the strength of concrete is less than that of limestone, so the energy required for the sawtooth fracture of concrete is less than that of the rock sawtooth fracture energy. When the groove width is 3.0 mm, the energy dissipation rate of all specimens is also the smallest. Because in the dynamic loading, the time used for the loading process is very short. Therefore, the loading time of all test specimens is very close, and the variation trend of dissipated energy and energy dissipation rate with different widths of interface groove is very similar, as shown in Figs. 13(e) and (f). When the groove width is 5.0 mm (the red curve in Fig. 13), the dissipated energy of the specimens rises significantly. However, when the groove width is 8.0 mm (the blue curve in Fig. 13), the dissipated energy of the specimens does not increase significantly.

4 Discussion

In actual engineering projects, artificial grooves are made on the surface of the rock to increase the roughness of the rock surface to improve the bonding performance of the rock−concrete interface. Because concrete and rock are two different materials, the stress state at the interface is more complicated than that of a single material. If the optimal groove width can be designed according to the mechanical properties of the rock or concrete, the safety and durability of the structure can be effectively ensured.

In order to obtain the most suitable groove width on the rock, a series of groove widths on the rock surface (that is, the width of the concrete sawtooth) were designed. If the groove width is too small and the ultimate bearing capacity of the concrete sawtooth is reached, then only the concrete sawtooth will fracture. However, if the groove width is too large and the ultimate bearing capacity of the rock sawtooth is reached only, then only the rock sawtooth fractures. When an appropriate groove width is set on the rock surface, the ultimate bearing capacity of the rock sawtooth can be equivalent to that of the concrete sawtooth, then the concrete sawtooth and rock sawtooth at the rock−concrete interface can fracture simultaneously.

The loads borne by the rock sawtooth and the concrete sawtooth at the interface are calculated by

$$F_r=\sigma_r A_r \tag{6}$$

$$F_c=\sigma_c A_c \tag{7}$$

where F_r and F_c are the ultimate loads borne by pure rock and concrete, respectively; σ_r and σ_c are the failure strengths of rock and concrete, respectively; A_r and A_c are the cross-sectional areas of rock or concrete, respectively.

When the rock−concrete structure is under load, the overall load resistance of the structure is the largest, that is, the loads on the rock sawtooth and the concrete sawtooth at the interface are the same, namely,

$$F_c=F_r \tag{8}$$

Since the rock−concrete interface is formed by the interlocking of rock sawtooth and concrete sawtooth, the total area of the interface (A_{sum}) is equivalent to the sum of the cross-sectional area of rock sawtooth and that of concrete sawtooth, as shown in Eq. (9):

$$A_{sum}=A_c+A_r \tag{9}$$

According to Eqs. (6)−(9), the cross-sectional areas of the rock and concrete sawteeth at the interface can be obtained by

$$A_r=\frac{\sigma_c}{\sigma_c+\sigma_r}A_{sum} \tag{10}$$

$$A_c=\frac{\sigma_r}{\sigma_c+\sigma_r}A_{sum} \tag{11}$$

In this study, the tensile strengths of the rock and the concrete are 4.83 and 2.06 MPa, respectively. The diameter of the disc specimen is about 50 mm and the thickness is about 25 mm. Because the interface passes through the center of the disk, the total area of the interface is 1250 mm^2.

Therefore, based on Eqs. (10) and (11), the total cross- sectional areas of rock and concrete sawteeth are 374 and 876 mm^2, respectively. Because the thickness of the disc specimen is about 25 mm, in the disc specimen in this test, the sum of the rock groove width is about 35 mm (the rock groove width is equal to the total cross-sectional area of the concrete sawtooth divided by the thickness of the disc specimen, so the sum of the length of the optimal groove width can be obtained as 35 mm). When the sum of the groove width is less than 35 mm, only the concrete sawtooth fractures. As shown in Fig. 14(a), the sum of the groove width of the specimen is about 21 mm, so the specimen only fractures along the concrete sawtooth. When the sum of the groove width is greater than 35 mm, the fracture of rock sawtooth occurs. The specimen in Fig. 14(b) has a total groove width of about 37 mm, so the fracture only occurs along the rock sawtooth.

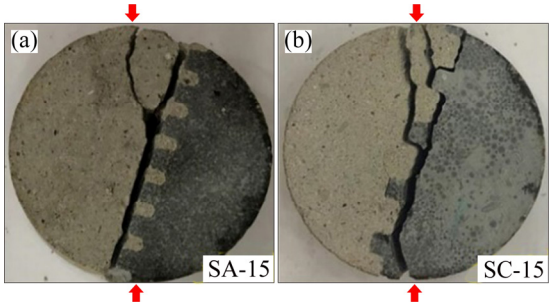

Fig. 14 Different groove widths on rock surface corresponding to different failure patterns of specimen: (a) 3 mm; (b) 8 mm

5 Conclusions

(1) When the interface inclination angle is 15°, the fracture pattern of the rock−concrete interface is significantly affected by the width of the interface groove. When the width of the rock−concrete interface groove is 3 mm, the concrete sawtooth at the interface is broken. However, when the width of the interface groove is 8 mm, the rock sawtooth at the interface is broken.

(2) The load−displacement responses are determined by the width of the interface groove. When the interface groove width is 3 mm, at the initial stage of loading, as the displacement increases, the corresponding load approximately increases linearly until it reaches the peak load. After the peak load, as the displacement continues to increase, the peak load suddenly drops to zero. When the groove width is 8 mm, before the peak load, the load gradually rises with the increase of the displacement. However, after the peak load, the load decreases stepwise as the displacement increases.

(3) The bearing capacity of structures containing rock−concrete interface is also closely related to the interface inclination angle θ and the interface groove width. If $0° \leq \theta \leq 30°$, the bearing capacity of the specimen rises first and then decreases with the increase of the width of the interface groove. Besides, the optimal groove width on the rock surface is 5 mm. If $45° \leq \theta \leq 90°$, the bearing capacity of the specimen tends to be stable with the increase of the width of the interface groove. Therefore, if the angle between the load direction and the interface direction is less than 45°, the bearing capacity of the structure can be effectively improved by properly increasing the width of the interface groove at the rock−concrete interface.

(4) The interface groove width has a significant effect on the dissipated energy of the specimen under dynamic loading. When the groove width is 3.0 mm, the dissipated energy of the specimen is the smallest. When the groove width is increased to 5.0 mm, the dissipated energy of the specimen rises significantly. However, if the groove width is increased to 8.0 mm, the dissipated energy of the specimen does not rise significantly.

Acknowledgments

The work is supported by the National Natural Science Foundation of China (No. 41772313), the National Natural Science Foundation for Young Scientists of China (No. 52104111), the Hunan Science and Technology Planning Project, China (No. 2019RS3001), the Natural Science Foundation of Hunan Province, China (No. 2021JJ30819), and Key Science and Technology Project of Guangxi Transportation Industry (Research on fine blasting and disaster control technology of mountain expressway tunnel), China. The authors are very grateful to the financial contribution and convey their appreciation for supporting this basic research.

References

[1] LUO Yan-bin, CHEN Jian-xun, SHI Zhou, LI Ju-zhu, LIU Wei-wei. Mechanical characteristics of primary support of

large span loess highway tunnel: A case study in Shaanxi Province, Loess Plateau, NW China primary [J]. Tunnelling and Underground Space Technology, 2020, 104: 103532.

[2] BJURELAND W, JOHANSSON F, SJÖLANDER A, SPROSS J, LARSSON S. Probability distributions of shotcrete parameters for reliability-based analyses of rock tunnel support [J]. Tunnelling and Underground Space Technology, 2019, 87: 15−26.

[3] BRYNE L E, ANSELL A, HOLMGREN J. Laboratory testing of early age bond strength of shotcrete on hard rock [J]. Tunnelling and Underground Space Technology, 2014, 41: 113−119.

[4] XIAO Peng, LI Di-yuan, ZHAO Guo-yan, LIU Huan-xin. New criterion for the spalling failure of deep rock engineering based on energy release [J]. International Journal of Rock Mechanics and Mining Sciences, 2021, 148: 104943.

[5] TIAN Hong-ming, CHEN Wei-zhong, YANG Dian-sen, YANG Jian-ping. Experimental and numerical analysis of the shear behaviour of cemented concrete–rock joints [J]. Rock Mechanics and Rock Engineering, 2015, 48(1): 213−222.

[6] PANG Bo, SAURÍ SUÁREZ H, BECKER F. Monte Carlo based study of radiation field in a deep geological repository for high-level nuclear waste with different host rock types [J]. Nuclear Engineering and Design, 2017, 325: 44−48.

[7] FISHMAN Y A. Stability of concrete retaining structures and their interface with rock foundations [J]. International Journal of Rock Mechanics and Mining Sciences, 2009, 46(6): 957−966.

[8] FISHMAN Y A. Features of shear failure of brittle materials and concrete structures on rock foundations [J]. International Journal of Rock Mechanics and Mining Sciences, 2008, 45(6): 976−992.

[9] DU Xue-ming, FANG Hong-yuan, WANG Shan-yong, XUE Bing-han, WANG Fu-ming. Experimental and practical investigation of the sealing efficiency of cement grouting in tortuous fractures with flowing water [J]. Tunnelling and Underground Space Technology, 2021, 108: 103693.

[10] ZHOU Jia-quan, ZHOU Chuan-bo, FENG Qing-gao, GAO Tan. Analytical model for load–transfer mechanism of rock–socketed drilled piles: Considering bond strength of the concrete–rock interface [J]. International Journal of Geomechanics, 2020, 20(6): 1−10.

[11] JOHNSTON I W, LAM T S K, WILLIAM A F. Socketed pile design in weak rock [J]. Geotechnique, 1987(1): 83−89.

[12] XING Hao-feng, LIU Liang-liang, LUO Yong. Effects of construction technology on bearing behaviors of rock-socketed bored piles as bridge foundations [J]. Journal of Bridge Engineering, 2019, 24(4): 2−10.

[13] KROUNIS A, JOHANSSON F, LARSSON S. Shear strength of partially bonded concrete–rock interfaces for application in dam stability analyses [J]. Rock Mechanics and Rock Engineering, 2016, 49: 2711−2722.

[14] DE GRANRUT M, SIMON A, DIAS D. Artificial neural networks for the interpretation of piezometric levels at the rock−concrete interface of arch dams [J]. Engineering Structures, 2019, 178: 616−634.

[15] FRIGERIO PORTA G, BEBBINGTON M, XIAO X, JONES G. Bayesian lifetime analysis for landslide dams [J]. Landslides, 2020, 17(8): 1835−1848.

[16] ZHONG Qi-ming, CHEN Sheng-shui, FU Zhong-zhi, SHAN Yi-bo. New empirical model for breaching of earth–rock dams [J]. Natural Hazards Review, 2020, 21(2): 06020002.

[17] QIU Hao, ZHU Zhe-ming, WANG Meng, WANG Fei, LUO Cai-song, WAN Duan-ying. Study of the failure properties and tensile strength of rock-mortar interface transition zone using bi-material Brazilian discs [J]. Construction and Building Materials, 2020, 236: 117551.

[18] ZHU Jian-bo, BAO Wei-yue, PENG Qi, DENG Xi-fei. Influence of substrate properties and interfacial roughness on static and dynamic tensile behaviour of rock-shotcrete interface from macro and micro views [J]. International Journal of Rock Mechanics and Mining Sciences, 2020, 132: 104350.

[19] ZHAO Bao-yun, LIU Yang, LIU Dong-yan, HUANG Wei, WANG Xiao-ping, YU Gui-bao, LIU Shu. Research on the influence of contact surface constraint on mechanical properties of rock−concrete composite specimens under compressive loads [J]. Frontiers of Structural and Civil Engineering, 2020, 14(2): 322−330.

[20] SELÇUK L, AŞMA D. Experimental investigation of the rock−concrete bi materials influence of inclined interface on strength and failure behavior [J]. International Journal of Rock Mechanics and Mining Sciences, 2019, 123: 104119.

[21] HONG Li, GU Xiang-lin, LIN Feng. Influence of aggregate surface roughness on mechanical properties of interface and concrete [J]. Construction and Building Materials, 2014, 65: 338−349.

[22] SON M. Adhesion strength at the shotcrete-rock contact in rock tunneling [J]. Rock Mechanics and Rock Engineering, 2013, 46(5): 1237−1246.

[23] ZHONG Hong, OOI E T, SONG Chong-min, DING Tao, LIN Gao, LI Hong-jun. Experimental and numerical study of the dependency of interface fracture in concrete-rock specimens on mode mixity [J]. Engineering Fracture Mechanics, 2014, 124/125: 287−309.

[24] DONG Wei, WU Zhi-min, ZHOU Xiang-ming, WANG Na, KASTIUKAS G. An experimental study on crack propagation at rock−concrete interface using digital image correlation technique [J]. Engineering Fracture Mechanics, 2017, 171: 50−63.

[25] DONG Wei, YANG Dong, ZHANG Bin-sheng, WU Zhi-min. Rock−concrete interfacial crack propagation under mixed mode I−II fracture [J]. Journal of Engineering Mechanics, 2018, 144(6): 1−12.

[26] CHANG Xu, LU Jian-you, WANG Shan-yong, WANG Shu-ren. Mechanical performances of rock−concrete bi-material disks under diametrical compression [J]. International Journal of Rock Mechanics and Mining Sciences, 2018, 104: 71−77.

[27] CHANG Xu, GUO Teng-fei, ZHANG Sheng. Cracking behaviours of layered specimen with an interface crack in Brazilian tests [J]. Engineering Fracture Mechanics, 2020, 228: 106904.

[28] ZHOU Zi-long, LU Jian-you, CAI Xin. Static and dynamic tensile behavior of rock−concrete bi-material disc with different interface inclinations [J]. Construction and Building Materials, 2020, 256: 119424.

[29] QIU Jia-dong, LUO Lin, LI Xi-bing, LI Di-yuan, CHEN Ying, LUO Yong. Numerical investigation on the tensile fracturing behavior of rock-shotcrete interface based on discrete element method [J]. International Journal of Mining Science and Technology, 2020, 30(3): 293−301.

[30] ANDJELKOVIC V, PAVLOVIC N, LAZAREVIC Z, NEDOVIC V. Modelling of shear characteristics at the concrete−rock mass interface [J]. International Journal of Rock Mechanics and Mining Sciences, 2015, 76: 222−236.
[31] MOUZANNAR H, BOST M, LEROUX M, VIRELY D. Experimental study of the shear strength of bonded concrete–rock interfaces: Surface morphology and scale effect [J]. Rock Mechanics and Rock Engineering, 2017, 50(10): 2601−2625.
[32] GUTIÉRREZ-CH J G, SENENT S, MELENTIJEVIC S, JIMENEZ R. Distinct element method simulations of rock−concrete interfaces under different boundary conditions [J]. Engineering Geology, 2018, 240: 123−139.
[33] ZHAO Wu-sheng, CHEN Wei-zhong, ZHAO Kun. Laboratory test on foamed concrete−rock joints in direct shear [J]. Construction and Building Materials, 2018, 173: 69−80.
[34] RENAUD S, SAICHI T, BOUAANANI N, MIQUEL B, QUIRION M, RIVARD P. Roughness effects on the shear strength of concrete and rock joints in dams based on experimental data [J]. Rock Mechanics and Rock Engineering, 2019, 52(10): 3867−3888.
[35] SHEN Yan-jun, WANG Yong-zhi, YANG Yang, SUN Qiang, LUO Tao, ZHANG Huan. Influence of surface roughness and hydrophilicity on bonding strength of concrete−rock interface [J]. Construction and Building Materials, 2019, 213: 156−166.
[36] HUANG L Q, WANG J, MOMENI A, WANG S F. Spalling fracture mechanism of granite subjected to dynamic tensile loading [J]. Transactions of Nonferrous Metals Society of China, 2021, 31: 2116−2127.
[37] LONG Yi, LIU Jian-po, LEI Gang, SI Ying-tao, ZHANG Chang-yin, WEI Deng-cheng, SHI Hong-xu. Progressive fracture processes around tunnel triggered by blast disturbances under biaxial compression with different lateral pressure coefficients [J]. Transactions of Nonferrous Metals Society of China, 2020, 30: 2518−2535.
[38] LI Xi-bing, QIU Jia-dong, ZHAO Yu-zhe, CHEN Zheng-hong, LI Di-yuan. Instantaneous and long-term deformation characteristics of deep room-pillar system induced by pillar recovery [J]. Transactions of Nonferrous Metals Society of China, 2020, 30: 2775−2791.
[39] TAN Li-hai, REN Ting, DOU Lin-ming, CAI Xin, YANG Xiao-han, ZHOU Qing-long. Dynamic response and fracture evolution of marble specimens containing rectangular cavities subjected to dynamic loading [J]. Bulletin of Engineering Geology and the Enironment, 2021, 80: 7701−7716.
[40] LUO Lin, LI Xi-bing, TAO Ming, DONG Long-jun. Mechanical behavior of rock−shotcrete interface under static and dynamic tensile loads [J]. Tunnelling and Underground Space Technology, 2017, 65: 215−224.
[41] LI X B, LOK T S, ZHAO J, ZHAO P J. Oscillation elimination in the Hopkinson bar apparatus and resultant complete dynamic stress−strain curves for rocks [J]. International Journal of Rock Mechanics and Mining Sciences, 2000, 37(7): 1055−1060.
[42] SHU Rong-hua, YIN Tu-bing, LI Xi-bing, YIN Zhi-qiang, TANG Li-zhong. Effect of thermal treatment on energy dissipation of granite under cyclic impact loading [J]. Transactions of Nonferrous Metals Society of China, 2019, 29: 385−396.
[43] WANG Pin, YIN Tu-bing, HU Bi-wei. Dynamic tensile strength and failure mechanisms of thermally treated sandstone under dry and water-saturated conditions [J]. Transactions of Nonferrous Metals Society of China, 2020, 30: 2217−2238.
[44] ZHOU Zi-long, CAI Xin, MA Dan, DU Xue-ming, CHEN Lu, WANG Hai-quan, ZANG Hai-zhi. Water saturation effects on dynamic fracture behavior of sandstone [J]. International Journal of Rock Mechanics and Mining Sciences, 2019, 114: 46−61.
[45] DAI F, XIA K, ZUO J P, ZHANG R, XU N W. Static and dynamic flexural strength anisotropy of Barre granite [J]. Rock Mechanics and Rock Engineering, 2013, 46(6): 1589−1602.
[46] JIANG F C, VECCHIO K S. Hopkinson bar loaded fracture experimental technique: A critical review of dynamic fracture toughness tests [J]. Applied Mechanics Reviews, 2009, 62(6): 1−39.
[47] XU Yuan, DAI Feng. Dynamic response and failure mechanism of brittle rocks under combined compression–shear loading experiments [J]. Rock Mechanics and Rock Engineering, 2018, 51(3): 747−764.
[48] ZHOU Zi-long, CAI Xin, LI Xi-bing, CAO Wen-zhuo, DU Xue-ming. Dynamic response and energy evolution of sandstone under coupled static–dynamic compression: Insights from experimental study into deep rock engineering applications [J]. Rock Mechanics and Rock Engineering, 2020, 53(3): 1305−1331.

界面形态对双材料圆盘的动态行为和能量耗散的影响

周子龙，陆建友，蔡 鑫，芮艺超

中南大学 资源与安全工程学院，长沙 410083

摘 要：为了研究岩石−混凝土界面的动态行为和能量耗散，采用霍普金森压杆对双材料圆盘进行动态劈裂试验。结果表明，随着界面倾角(θ)的变化，界面槽宽度对试件承载力的影响也发生变化。当θ从 0°增加到 30°时，试样的承载力随界面槽宽度的增加先增大后减小；在此界面倾角范围内，岩石表面的最佳刻槽宽度为 5 mm。当θ从 45°增加到 90°时，试样的承载力没有明显变化。当θ从 0°增大到 45°时，随着界面槽宽度的增大，试样的耗散能先明显增加，然后趋于稳定。

关键词：岩石−混凝土界面；巴西劈裂；裂隙发育；界面力学性能；动态行为；能量耗散

(Edited by Xiang-qun LI)